J Mater Sci (2011) 46:6889–6896
DOI 10.1007/s10853-011-5653-y

Inkjet printing of gadolinium-doped ceria electrolyte on NiO-YSZ substrates for solid oxide fuel cell applications

Chingfu Wang · Rumen I. Tomov · R. Vasant Kumar · Bartek A. Glowacki

Received: 18 January 2011 / Accepted: 24 May 2011 / Published online: 4 June 2011

Abstract A sol–gel-based precursor solution of gadolinium-doped ceria (CGO) was developed for deposition by inkjet printing. A stable precursor was synthesised by dissolving stoichiometric amounts of cerium (III) acetate hydrate and gadolinium (III) acetate hydrate in propionic acid, and diluted to 0.75 M with 1-propanol. The sintering behaviour of the printed precursor was investigated. Since the commonly used method of dilatometry is only applicable to bulk samples, an alternative approach using Differential scanning calorimetry (DSC) has been explored. The sintering temperature of the printed precursor was estimated by subtracting contributions from energy stored due to heat capacity and activation energy of ionic mobility from the DSC heat flow signal. Based on this modelling it was found that the optimum sintering temperature of the acetate-based CGO precursor was 1100 ± 55 °C, a result independently confirmed by SEM imaging of printed precursor coating on NiO-YSZ cermet. A gadolinium-doped ceria (CGO) thin film was then directly deposited on a porous NiO-YSZ cermet anode composite by inkjet printing. After co-sintering, it was shown that crack-free and continuous coating thinner than 10 μm of CGO can be readily produced. These results suggest that the inkjet printing technique can be successfully implemented to fabricate a thin film of dense electrolyte (>98%) for solid oxide fuel cell (SOFC) applications.

C. Wang (✉) · R. I. Tomov · R. Vasant Kumar · B. A. Glowacki
Material Chemistry and Applied Superconductivity Group, Department of Materials Science and Metallurgy, University of Cambridge, Pembroke Street, Cambridge CB2 3QZ, UK
e-mail: cw427@cam.ac.uk

Introduction

Gadolinium-doped ceria (CGO) is a promising electrolyte material for intermediate temperature (below 600 °C) solid oxide fuel cells (IT-SOFC) due to its high ionic conductivity and adequate chemical stability [1]. The electrolyte layer must be gas-tight in order to prevent mixing of the fuel and the oxidant, and sufficiently thin to minimise ohmic resistance. The ideal electrolyte layer has to be dense without any porosity, so that the conducting cross-section is maximised. In SOFC development a serious effort has been devoted to creating a dense, thin electrolyte. There are two main categories of processing routes which are sufficiently cost-effective to be considered, one being the conventional ceramic powder route and the other being the chemical route.

The former technique employs sub-micron ceramic particles prepared as a stable colloidal suspension in the form of a slurry or paste. The suspension can then be deposited on the substrate with commonly used deposition methods such as screen printing [2, 3] or tape casting [4]. However, the conventional technique requires a high sintering temperature compared with chemical route (above 1300 °C, due to the relatively coarse particles size ranging from 0.5 to 5 μm, often further accentuated by agglomeration), and the reliable deposition of coatings with thicknesses less than 10 μm by these methods presents a challenge. Relatively high sintering temperature is particularly problematic since the anode layer will undergo sintering as well, resulting in a reduction in its porosity leading to high concentration polarisation losses during fuel cell operation.

Hence, an increasing trend is towards development of chemical techniques based on sol–gel route. A chemical sol precursor can be made by dissolving metal salts in suitable

solvents to create fine, agglomerate-free particles which potentially can uniformly disperse in the chemical precursor. Owing to the resulting nanometric scale particle size the sintering temperature can be significantly lowered [5].

The solution can be deposited by various chemical solution deposition techniques, such as spray pyrolysis [6, 7] or spin coating [8]. However, the major drawback of these techniques is the large volume reduction due to solvent loss, which results in cracks formation, making this technique difficult to implement [9]. These effects are characteristic for the above mentioned techniques due to an insufficient level of control in the lateral and vertical spatial distribution of the solution. For instance, spray pyrolysis suffers from a "stacking effect" where small droplets preferentially land on top of one another, leading to uneven thickness and cracking during annealing [10]. A lateral effect is witnessed in spin coating, where the thickness varies radially being smallest in the centre due to the centrifugal force, which also results in crack formation.

Drop-on-demand inkjet printing offers an attractive alternative to overcome such problems offering several key advantages over conventional chemical solution deposition techniques. It allows much greater control of the coating thickness by depositing the exact amount of material required at the desired position, so a uniform coating can be achieved. It also introduces the possibility of printing homogeneous coatings as well as graded structures. This is particular useful in the SOFC application where a thin dense film (electrolyte) on a graded pore structure (electrode) can be fabricated by a single technique [11].

In this study, the use of DSC to determine the sintering behaviour of a chemical solution-based precursor is reported. Sintering conditions are critical to the success of the film, in order to fully densify the electrolyte without adversely impairing the porous structure of the anode or encouraging interfacial reactions. Ideally, it is desirable to use the lowest possible temperature at which the specifications are readily met. In addition, inkjet printing is demonstrated as an attractive alternative chemical solution deposition method capable of producing thin films on a porous substrate using a chemical precursor.

Experimental

Precursor preparation and solvent selection

The $Ce_{0.9}Gd_{0.1}O_{1.95-x}$ precursor solution (1.5 M total metal concentration) was prepared by dissolving cerium (III) acetate hydrate (99.9%, Sigma-Aldrich) and gadolinium (III) acetate hydrate (99%, Sigma-Aldrich) in two steps in propionic acid (99.9%, Sigma-Aldrich) under reflux for 4 h at 120°C [12]. The solution was then cooled to room temperature. The obtained precursor was then filtered through a 0.3 μm polypropylene membrane syringe filter (Whatman) in order to eliminate the possibility that particles of dust or other contaminants remained to block the nozzle of the inkjet print-head. The precursor was further diluted in order to reduce the viscosity to a level suitable for printing. Suitable viscosity level was determined by printing the inks directly. The viscosity of volume ratio 1:1 (precursor: solvent) was low enough to be printed under 0.5 bars with 300 μs opening time and to produce stable droplets. A solvent with high volatility is desirable, since such solvents evaporate instead of decomposing and leaving a concentrated residue behind. Evaporating solvents effectively increases the packing density of the particles. The solvent should be miscible with the starting precursor while maintaining its stability such that no precipitates form. A number of different solvent/precursor mixtures were tested to evaluate stability of the ink, which was determined by observing any formation of precipitation after the mixture was left to rest for 24 h. From amongst the solvent tested, 1-propanol was selected as the diluent to make a stable printable ink (0.75 M).

Inkjet printing parameter optimisation

The printer used for this experiment consists of an electromagnetic single nozzle print-head with 90 μm ruby orifice, modified from a Domino MacroJet printer, mounted 10 mm above the substrate on a Roland plotter as shown in Fig. 1. The print head is based on the operation of an electromagnetic solenoid valve. Precursor solution is delivered under pressure of 0.6 bar to a reservoir which is sealed by a rubber-tipped piston. An electrical pulse passed through the solenoid generates a magnetic field to drive the piston up and down. A given length of electrical pulse can lift the piston from the orifice for a selected amount of time, which is termed the "opening time" parameter, and a volume of the suspension is then ejected from the nozzle, forming a droplet. The volume of the droplet is expected to vary approximately linearly with the opening time. Such external solenoid design is beneficial for separating the sol/suspension ink in the print chamber from the heat generated by the solenoid; hence parameters such as viscosity can be kept constant. It is worth noting that below a certain opening time (250 μs), no individual droplets can be released from nozzle due to retardation from capillary force. The jetting parameters were optimised (a detailed optimization method is described elsewhere [13]). The optimum pressure was found to be 0.6 bar relative to atmospheric pressure, with an opening time of 350 μs, resulting in a drop on the substrate approximately 500 μm in diameter, as shown in Fig. 2.

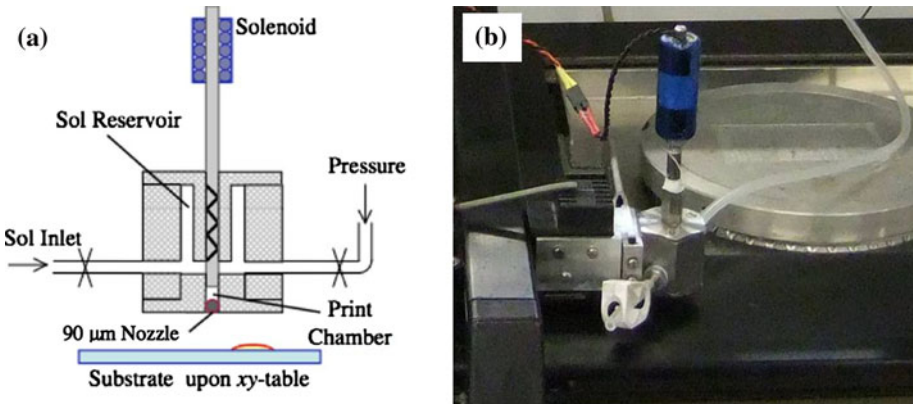

Fig. 1 The custom-built drop-on-demand inkjet print-head. **a** Schematic of the print head, **b** photograph of the configuration for printing on a hot plate

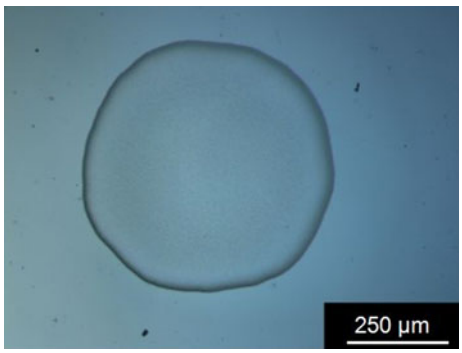

Fig. 2 Single droplet of gadolinium-doped ceria precursor on a glass slide, showing uniform spreading and without precipitation

A complete coating was deposited on a tape-cast cermet NiO-YSZ substrate which was manufactured and pre-sintered at 1100 °C with a porosity of 25% (Institute of Power Engineering, Ceramic Department, CEREL, Poland) [14]. The substrate was placed on the hot plate at 100 °C mounted on the plotter. The flow of heat to the printed material is expected to reduce the extent of drying stress during evaporation of the solvent, as solvent can evaporate when drops just contact the substrate surface. A square array of droplets with a spacing of 0.4 mm was used in such a manner to provide complete coverage. A total of ten layers were deposited with an intermediate heat treatment between every layer.

Formation of CGO film on a NiO-YSZ substrate

Intermediate heat treatment

After the printing of each layer, the sample was placed on a hot plate at an intermediate temperature of 400 °C in order to get rid of the majority of organic residue in the as-deposited film. The burn out of organic residue effectively allows for a high packing density of the particles in the film.

Heat treatment

The heating rate was 5 °C/min to 650 °C to ensure all possible organic residues can be decomposed. After 1 h at 650 °C, the furnace was then ramped (5 °C/min) to the final sintering temperatures which were then held for 2 h. Three set of samples were sintered at three different temperatures, 900, 1000, and 1100 °C, selected based on the computed DSC result (see Results and discussion). All samples were sintered in air.

It is worth noting that after stinting the ceramic stoichiometry is $Ce_{0.9}Gd_{0.1}O_{1.95}$. Since the sample is sintered in an oxygen rich environment of air and it is widely accepted that the final composition stoichiometry of the sintered CGO in air is $Ce_{0.9}Gd_{0.1}O_{1.95}$, rather than $Ce_{0.9}Gd_{0.1}O_{1.95-x}$ (oxygen deficient) especially at temperatures below 600 °C. The Ce(IV)/Ce(III) ratio increases with decreasing temperature at any given oxygen pressure. The valence of Ce in $Ce_{0.9}Gd_{0.1}O_{1.95}$ stoichiometry is 4+ below 600 °C at the nominal operating temperature of SOFC that use CGO as electrolyte hence we have assumed that the Ce is in 4+ state.

Characterisation

Thermogravimetry (TG) was performed on the chemical precursor to determine the decomposition behaviour using a TA Instruments TGA Q500 with a heating rate of 5 °C/min from room temperature to 600 °C using a Pt crucible in air. Since the sample is not bulk, conventional sintering analysis which measures the dimensional changes of a powder compact against temperature is not suitable. An alternative method is to use DSC to investigate sintering behaviour, as DSC can measure heat flow of the samples upon heating, which can provide an indication of the processes/reactions taking place in the temperature range. DSC analyses were performed using a TA Instruments SDT Q600 with a heating rate of 10 °C/min from room temperature to 1300 °C using an alumina crucible in

air. Two samples were subject to DSC heat flow measurement, one being the CGO precursor solution sample, the other being CGO particle obtained after sintered the CGO precursor at 1500 °C for 4 h.

The morphology of each sample was examined by field emission gun SEM (JEOL 6420), and the SEM images were then individually thresholded to produce binary images using ImageJ in order to quantify the surface porosity.

Results and discussion

High resolution TG was conducted on the ink in order to determine the intermediate heat treatment temperature. Intermediate heat treatment between each coating is a critical step for the coating formation, as the removal of organic residue will effectively help pack the particle more densely. Propensity to cracking can be greatly reduced by quickly removing liquid in the space between particles [15]. Above 400 °C there was insignificant mass reduction, suggesting that almost of organics were removed (Fig. 3).

Majority of the organic components had decomposed or evaporated below 400 °C, and an intermediate heat treatment temperature was selected based on this result. Intermediate heat treatment is essential as it removes the organic residue to prevent drying cracks and increase the packing density of the particles.

The DSC results (Fig. 4) show heat flow characteristic feature that can be distinguished when comparing sintered sample and precursor (non-sintered) sample. The results for the $Ce_{0.9}Gd_{0.1}O_{1.95}$ precursor show a broad peak at 1200 °C as well as a small bump close to 480 °C which is assumed to be crystallisation peak [16, 17]. Crystallisation peak appear to be very sharp and is attributed to the small grain size. Whereas for sintered $Ce_{0.9}Gd_{0.1}O_{1.95}$ samples there is no similar peak that can be seen. The curve for sintered $Ce_{0.9}Gd_{0.1}O_{1.95}$ samples is initially a straight line and a transition occurs at around 900 °C. It is expected that in the sintered $Ce_{0.9}Gd_{0.1}O_{1.95}$ sample, there would be no further sintering occurring so no peak should appear and heat flow to be endothermic.

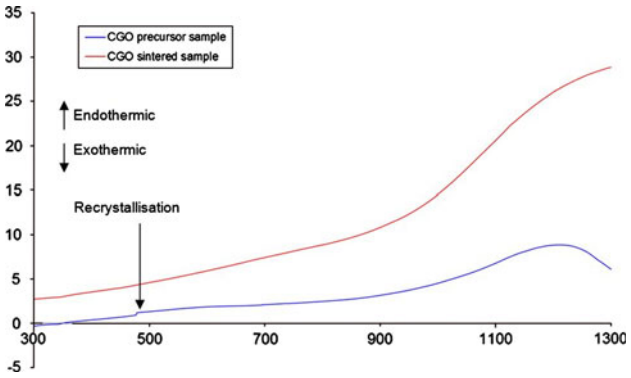

Fig. 4 DSC results for the $Ce_{0.9}Gd_{0.1}O_{1.95}$ precursor and a $Ce_{0.9}Gd_{0.1}O_{1.95}$ sintered sample. The sintered sample had been annealed at 1500 °C for 4 h

However, the DSC results for $Ce_{0.9}Gd_{0.1}O_{1.95}$ precursor (Fig. 4) also only includes endothermic features, despite the fact that the densification (final stage of sintering) process is known to be an exothermic process due to the release of surface energy. This can be explained by the existence of endothermic processes occurring simultaneously with sintering processes which dominate over the heat release, consequently masking the heat evolution signal from the sintering process. Hence the endothermic contributions need to be identified and estimated, and then subtracted from the DSC signal. This would allow the true sintering process DSC data to be obtained and the sintering temperature of $Ce_{0.9}Gd_{0.1}O_{1.95}$ to be estimated as described in Eq. 1.

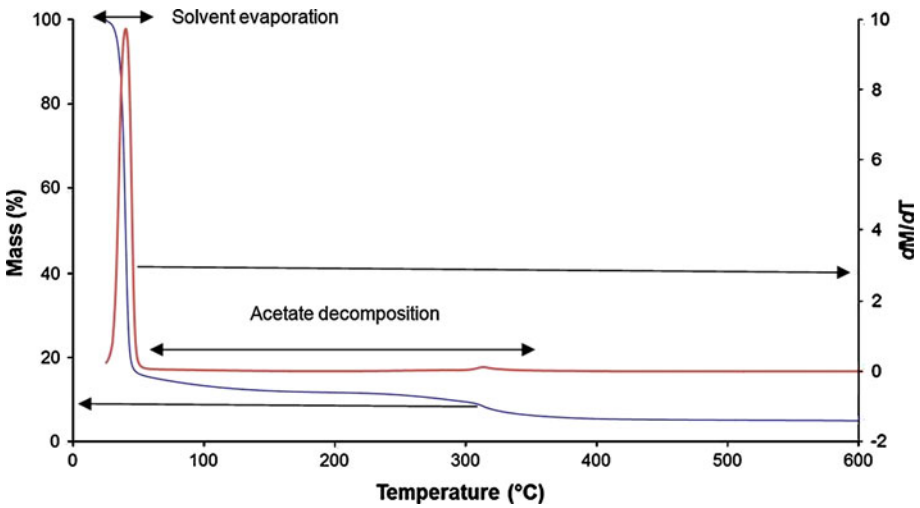

Fig. 3 High resolution thermogravimetry results, showing decomposition of the gadolinium-doped ceria precursor

$$\frac{dE_{sintering}}{dt} = \frac{dE_{total}}{dt} - \frac{dE_{C_p}}{dt} + \frac{dE*}{dt} \quad (1)$$

Two main endothermic contributions in $Ce_{0.9}Gd_{0.1}O_{1.95}$ are expected to be energy absorbed and stored in $Ce_{0.9}Gd_{0.1}O_{1.95}$ due to heat capacity E_{C_p}(J) and the energy required to activate ionic motion know as activation energy of ionic mobility E*(mol^{-1} J^{-1}). $\frac{dE_{total}}{dt}$ (W) is equal to DSC heat flow signal which the rate at which heat is absorbed as the sample is heated at 10 °C/min. The specific heat capacity is a function of temperature and can be describe by Eq. 2. The energy absorbed by $Ce_{0.9}Gd_{0.1}O_{1.95}$ can then be written by Eq. 3, where C_p can be substituted by Eq. 2 [18].

$$C_p = 9.80 \times 10^{-2}T + 423 \quad (2)$$

$$\frac{dE_{C_p}}{dt} = C_p \times m \times \frac{dT}{dt} \quad (3)$$

where C_p is the specific heat capacity (J/K) of $Ce_{0.9}Gd_{0.1}O_{1.95}$, m is mass (g), T is temperature (K), and t is time (s).

Another major endothermic process occurring is related to the energy require for oxygen ions to hop between vacancies. Activation energy of ionic mobility is a function of temperature: as the temperature increases, the hopping of oxygen ions occurs more frequently. The total energy release due to activation energy of ionic mobility can be calculated by Eq. 4,

$$\frac{dE*}{dt} = \frac{dE_m}{dT} \times \frac{dT}{dt} \quad (4)$$

where $\frac{dE*}{dT}$ (W) is the rate of activation energy change, ΔH_m is the activation enthalpy of ionic mobility (eV) Eq. 5.

$$E* = \frac{A}{T}\exp\left(-\frac{\Delta H*}{kT}\right) \quad (5)$$

where A is pre-exponential factor, and k is Boltzmann's constant. The activation energy of ionic mobility of $Ce_{0.9}Gd_{0.1}O_{1.95}$ is known to be 1.36 ± 0.04 eV [19].

There are 4 sets of data in Fig. 5: the blue line represent the raw DSC heat flow signal, the green line represent the heat flow attributed to heat capacity of CGO, the grey band represents calculated activation energy for ionic mobility (with error estimation, so any value within the grey band can be considered as acceptable value for activation energy for ionic mobility estimation), and the red band is the heat flow calculated by subtracting all of the endothermic heat flow (green line and red band) from the raw DSC data (blue line).

In this particular modelling, the energy associated with activation energy of ionic mobility greatly exceeds the heat capacity term from 800 to 900 °C, therefore the main

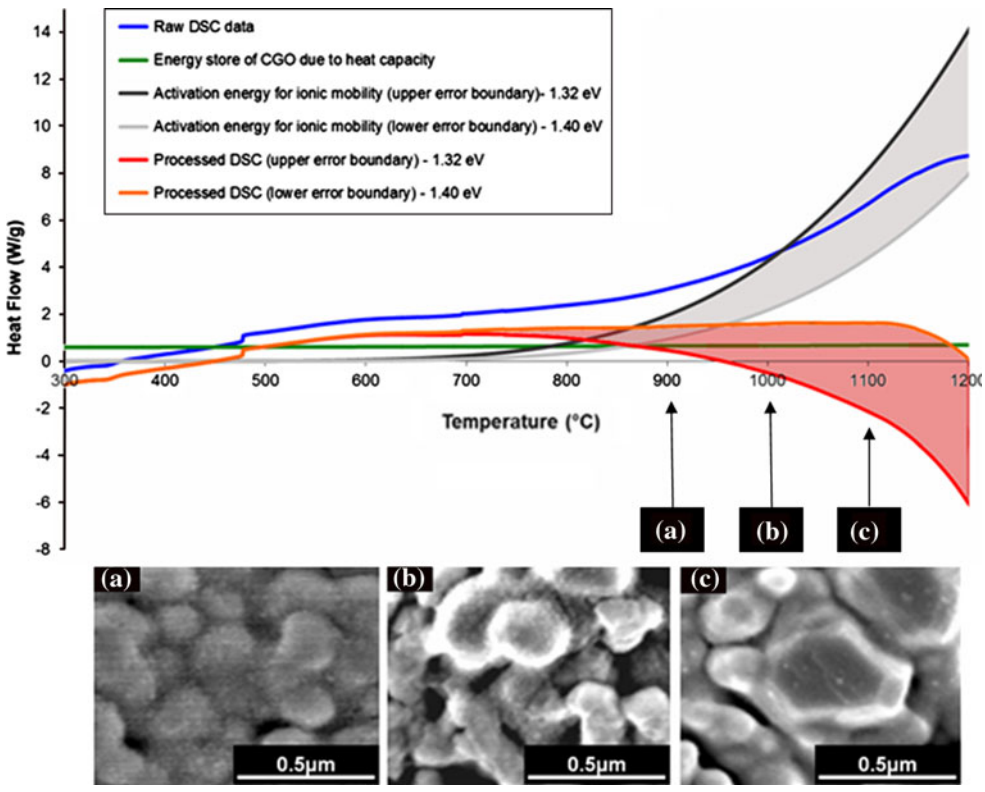

Fig. 5 DSC analyses and DSC computed analysis. FEGSEM images of coatings sintered at: **a** 900 °C **b** 1000 °C **c** 1100 °C

source of error is contributed by the activation energy of ionic mobility and the error of the heat capacity can be neglected since it does not contribute to the overall heat flow significantly. Two lines can be plotted by substituting the upper and lower bound value which are 1.32 and 1.40 eV, respectively, into the activation enthalpy of ionic mobility term in Eq. 5, giving a confidence range of ±5%. It is worth noting that the calculated lines for activation energy of ionic mobility (from Eq. 5) agree with the trend of DSC heat flow result of sintered $Ce_{0.9}Gd_{0.1}O_{1.95}$ samples: the feature at 900 °C in the DSC data coincides with increasing oxygen ions hopping between vacancies.

The insert SEM image shows different stages of sintering at (a) 900 °C (b) 1000 °C (C) 1100 °C, which coincide with the processed DSC result (red band). Since the result has been normalised, i.e. the resulting values after subtracting all endothermic processes (i.e. energy store due to heat capacity and ionic mobility) are considered. When the red band becomes negative, this point has been taken as the start of sintering since sintering is an exothermic process.

At low temperatures, the only strong signal is the feature at 480 °C attributed to crystallisation. At high temperatures, there is a broad exothermic feature corresponding to sintering, as expected. The onset of this feature (at which the heat flow gradient becomes negative) is at 820 °C for the lower bound data and 1100 °C for the upper bound, so 950 °C was taken to be a reasonable approximation of the lowest temperature suitable for sintering as shown on Fig. 5. Figure 6 shows the differential of activation energy of ionic mobility which the value is taken from the average of upper and lower bound, as it indicate the rate of exothermic change is greatest at 1100 °C which is most likely where substantial sintering is taking place.

Experimentally, samples were sintered at temperatures of 900, 1000, and 1100 °C for 1 h and examined by SEM (see Fig. 5). Figure 5a shows neck formation between particles at 900 °C. Figure 5b shows that, at 1000 °C, the neck has grown to a size similar to that of the particle. Figure 5c shows grains developing a tetrakaidecahedral form, indicating that intermediate and/or final stage sintering has begun. The early stage of sintering observed in Fig. 6a is consistent with the onset temperature estimated from analysis of the DSC data. In order to obtain a dense coating whilst avoid excess sintering of the substrate and reducing sintering time, it is therefore necessary to use a sintering temperature of 1100 °C. In conclusion, calculation form this model can be used to predict the sintering temperature of CGO sol precursor.

After the sintering temperature were evaluated from DSC data, complete coverage CGO coatings were deposited on porous NiO-CGO substrates with 50% surface porosity (Fig. 7). After the first deposition cycle (ten layer of deposition and then sintering at 1100 °C), the surface porosity of NiO-CGO substrate was reduced significantly to 5% (Fig. 8). Furthermore, there were no cracks found on the deposited CGO film. The pin holes on the surface of the CGO film are very much smaller than the surface pores of the NiO-CGO substrate: nano-size pores in comparison to the broad distribution of pore sizes, some exceeding 1 μm, of the initial substrate. With optimisation, this particular morphology could form a very useful structure for the electrode in an SOFC. After a second deposition cycle (another ten layers of deposition and then sintering at

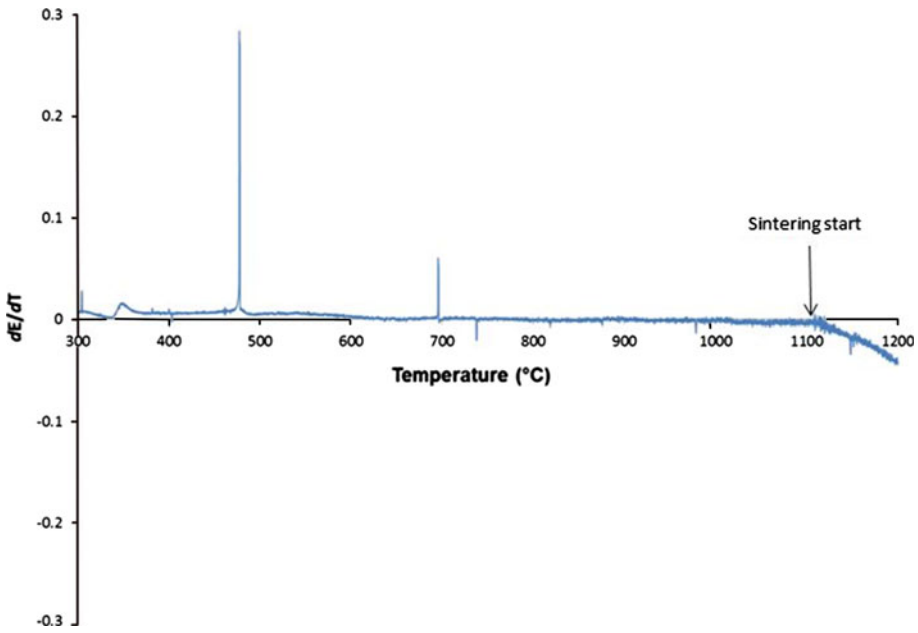

Fig. 6 The rate of heat flow of CGO precursor. As the *arrow* indicates, 1100 °C would be the starting of sintering. The value is the average of upper and lower bound processed DSC

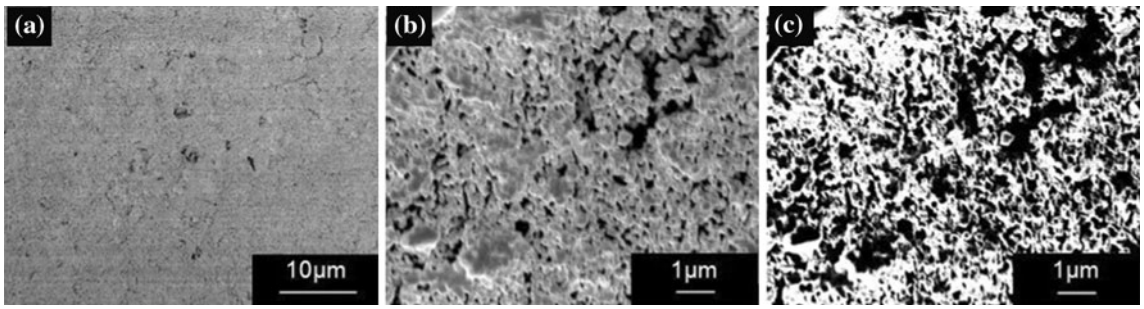

Fig. 7 SEM images of substrate: **a** top view, **b** enlargement of *white square* in (**a**), **c** binary thresholded image of (**b**) in order to estimate the pore density: the pore volume is 50%

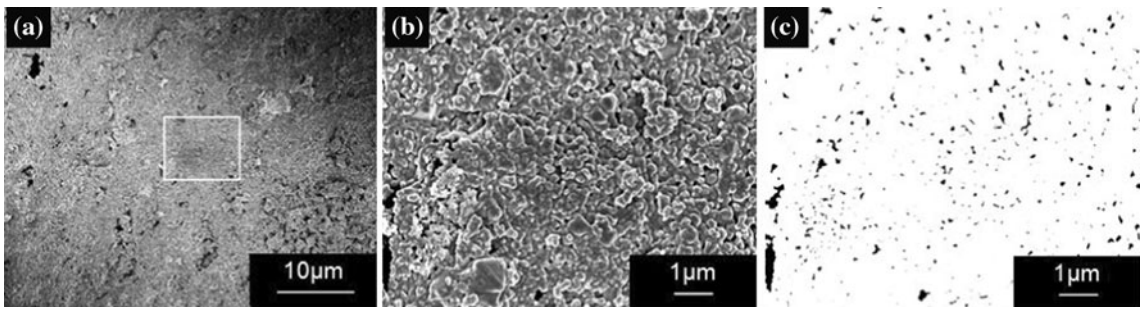

Fig. 8 SEM images of first (ten layers) deposition cycle of the precursor coating on the substrate and sintered at 1100 °C: **a** top view, **b** enlargement of *white square* in (**a**), **c** binary thresholded image indicating surface pore volume is 5%

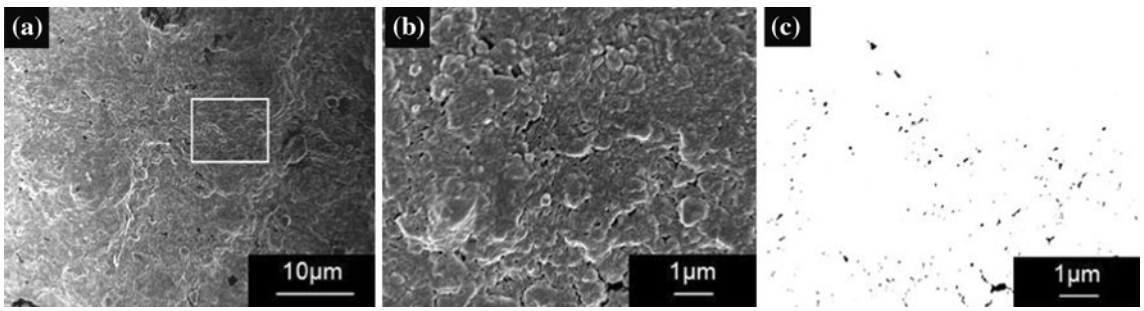

Fig. 9 SEM images second (ten layers deposition) cycle of the precursor coating and sintered at 1100 °C: **a** top view, **b** enlargement of *white square* in (**a**), **c** binary thresholded image indicating 2% of surface porosity

1100 °C), no obvious porosity was seen on the surface of CGO film, apart from some micro-size pores which are likely to have been caused by debris or dust. The binary image indicates that the surface porosity is of less than 2% (Fig. 9). It is likely that pores arising from dust are confined to the upper surface of the film, thus rendering such coatings, suitable for electrolyte layers.

The cross section view (Fig. 10) of the CGO film shows a dense thin film suspended on the surface of NiO-CGO porous substrate, although surface morphology of a sintered film on a ridge substrate usually appears to be denser than the interface, in this study, the density of the film appears to be uniform across its thickness. This may be the result of repeated cycle of printing and heat treatment, which allows the sol–gel precursor to infiltrate and create high-density particle packing of CGO prior to sintering and hence a dense film can be made. The infiltration is evidence in both where the thickness of the film is non uniform indicating different degrees of infiltration of the sol gel precursor. In addition there are some signs of delamination between the film and substrate and small crack on the surface of film. This is the result of constrain from the rigid substrate, since the substrate does not shrink, this effect can put the film under tension during sintering. The shrinkage

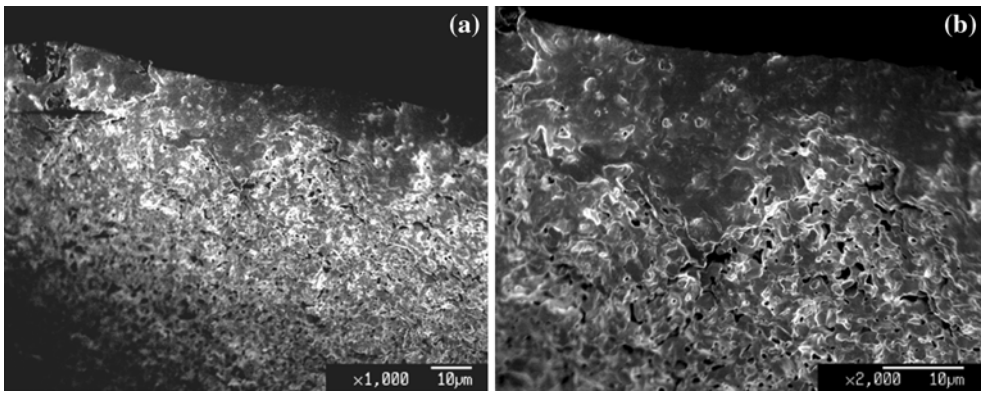

Fig. 10 The cross section view of the deposited film after two cycle CGO ink deposition **a** ×1000 magnification **b** ×2000 magnification

matching of the substrate and film has to be optimised and the constrain condition of substrate and printed film required further investigation.

Conclusion

It has been shown that DSC could be very useful in the study of sintering behaviour of a sol–gel-based precursor films where the conventional dilatometry method is not applicable. Based on the SEM and DSC result, it was shown that sintering process takes place around 1100 °C for the acetate-based precursor for CGO The optimum sintering temperature was estimated at 1100 °C in order to obtain a dense coating whilst avoiding long sintering times and excess sintering of the substrate. It has also been demonstrated that inkjet printing is a promising deposition route for sol–gel-based precursor to produce a thin, crack free, and dense coating.

Acknowledgements The Author would like to thanks to M. Klaus Institute of Power Engineering, Ceramic Department, CEREL, Poland, for proving materials for the experiments. Additional support goes to Kemlok. Co. for the financial funding of the project.

References

1. Steele BCH (2000) Solid State Ionic 129:51
2. Peng RR, Xia CR, Liu XQ, Peng DK, Meng GY (2002) Solid State Ionic 152–153:561
3. Ge X, Huang X, Zhang Y, Lua Z, Xua J, Chen K, Dong D, Liu Z, Miao J, Su W (2006) J Power Sour 159:1048
4. Fukui T, Ohara S, Murata K, Yoshida H, Miura K, Inagaki T (2002) J Power Sour 106:142
5. Prasad D, Kima H, Park J, Son J, Kim B-K, Lee H-W, Lee J-H (2010) J Alloys Comp 495:238
6. Will J, Mitterdorfer A, Kleinlogel C, Perednis D, Gauckler LJ (2000) Solid State Ionic 131:79
7. Rupp JLM, Gauckler LJ (2006) Solid State Ionic 177:2513
8. Chen CC, Nasrallah MM, Anderson HU (1994) Solid State Ionic 70–71:101
9. Atkinson A, Guppy RM (1991) J Mater Sci 26:3869. doi: 10.1007/BF01184984
10. Muecke UlrichP, Luechinger Norman, Schlagenhauf Lukas, Gauckler LudwigJ (2009) Thin Solid Film 517:1522
11. An C, Song J, Kang I, Sammes N (2010) J Power Sour 195:821
12. Mosiadz M, Tomov RI, Hopkins SC, Martin G, Hardeman D, Holzapfel B, Glowacki BA (2010) Sol Gel Sci Technol 54:154
13. Tomov RI, Krauz M, Jewulski J, Hopkins SC, Kluczowski JR, Glowacka DM, Glowacki BA (2010) Power Sour 195:7160
14. Golec T, Antunes R, Jewulski J, Miller M, Kluczowski R, Krauz M, Krzastek K, Blesznowski M (2010) J Fuel Cell Sci Technol 7(1):011003.1
15. Holmes DM, Kumar RV, Clegg WJ (2006) J Am Ceram Soc 89(6):1908
16. Bhuiyan MS, Paranthaman M, Sathyamurthy S, Aytug T, Kang S, Lee D, Goyal A, Payzant E, Salama K (2003) Supercond Sci Technol 16:1305
17. Chen S, Wang SS, Shi K, Liu Q, Han Z (2005) Physica C 419:7
18. Stelzer N, Nolting J, Riess I (1995) J Solid State Chem 117:392
19. Suzuki T, Kosacki I, Anderson HU (2002) J Am Ceram Soc 85(6):1492